

Non-linearities in the low-frequency dynamics of transitional shock wave / boundary layer interactions

Mariadebora Mauriello⁽¹⁾, Lionel Larchevêque⁽²⁾ and Pierre Dupont⁽³⁾

⁽¹⁾Aix-Marseille Univ, CNRS, IUSTI, Marseille, France, mariadebora.mauriello@univ-amu.fr

⁽²⁾Aix-Marseille Univ, CNRS, IUSTI, Marseille, France, lionel.larcheveque@univ-amu.fr

⁽³⁾Aix-Marseille Univ, CNRS, IUSTI, Marseille, France, pierre.dupont@univ-amu.fr

ABSTRACT

Large-eddy simulations (LES) of transitional shock wave boundary layer interactions (TrSBLIs) are carried out and results are compared with available experimental databases from the TFAST project. The separated region is characterised by low-frequency breathing and it is associated with a fluidic feedback originating from the vicinity of the reattachment point, in agreement with previous investigations. The non-linear spectral analysis revealed a quadratic coupling between the low-frequency feedback and the linear unstable modes developing within the mixing layer.

1. INTRODUCTION

Shock wave boundary layer interactions (SBLIs) have been subject of extensive investigations in the last 70 year [9]. Much of the interest has been devoted to interactions between shock waves and turbulent boundary layers and the necessity of understanding such flows has motivated numerous experimental, numerical and theoretical studies [12, 26, 3]. A large variety of geometric configurations have been covered such as normal shock interactions, incident-reflecting interactions, compression corner, over-expanded nozzle, etc., and investigations spanned a wide range of Mach and Reynolds numbers. The global organization in terms of space and time dynamics have been depicted [12] and the qualitative mean organisation of the flow is currently well understood [2]. In the case of turbulent separated SBLIs, evidence showed that the interaction is highly unsteady with very low-frequency motions of the separated region [10, 13, 12, 29]. Nevertheless, the origin of such phenomenon is still under debate and divides the scientific

community into different strands of thought. Multiple studies claim the upstream mechanism as a natural source of the low-frequency unsteadiness of the system such as broadband fluctuations [27], or the existence of superstructures in the incoming turbulent boundary layer which are required to induce the flapping of the separated region [13]. Other authors propose to correlate these unsteadiness with the dynamics of the separated region [29, 20], or with resonance mechanism in the interaction region [19]. Reference [18] developed a simple model to explain the low-frequency unsteadiness. It is based on the entrainment characteristics of the shear layer and relates the mass recharge within the separated bubble to the flapping dynamics occurring near to the reattachment point. However, a new consensus paved the way of uniting both upstream and internal mechanism as contributors to the emergence of the low-frequency unsteadiness, but the effect of the incoming turbulent layer diminishes for increasing interaction strengths [5].

Less attention has been devoted to interactions between shock waves and an incoming laminar boundary layer and only recently the scientific community has taken steps in that direction. The TFAST project carried out both numerical [4, 17] and experimental [8] studies on these unexplored transitional interactions. Their studies confirmed that unsteadiness comes up when transition to turbulence occurs. For example, the work of [22] revealed that as the breakdown of the turbulence occurs, broadband disturbances travel upstream in the subsonic region of the boundary layer with a corresponding response near the separation point. Further, temporal measurements revealed several frequencies being amplified along the interaction with the low frequency unsteadiness of the separation region being one order of magnitude higher than that found in the turbulent counterpart [7].

Reference [17] demonstrated that the region of reattachment might be the origin of the low-frequency unsteadiness and that their amplitude vary significantly with the size of the separated region and the location of the transition to turbulence. However, all of these studies agree to associate the low-frequency unsteadiness with a feedback originating from the reattachment region, although a lot of open questions are left unanswered.

The present work aims at better characterise the physical origin of the low-frequency unsteadiness leveraging the non-linear spectral analysis, a tool that suits well when dealing with quadratic interactions. In fact, it is shown that the linearly unstable modes found in the mixing layer and developing over the separation region quadratically link with the low-frequency feedback near the reattachment point.

2. NUMERICAL SIMULATIONS

2.1 Numerical setup

The datasets of the present numerical simulations are based on two TrSBLIs investigated in the experiments carried out in the TFAST project. The first one was performed at the IUSTI laboratory in Marseille [8]. The second setup corresponds to the experiments performed by [15] at TU Delft. Both investigations are carried out at Mach 1.7, but with different Reynolds numbers. The details are described in Tab. 1.

All simulations were performed using the FLU3M code from ONERA. The code relies on a finite volume discretisation in space and an implicit Gear scheme for the temporal discretisation, both being second-order accurate. To minimize the numerical dissipation, the space scheme is modified by adding the dissipative part of the Roe scheme to a centered scheme in regions where strong compressibility/low vorticity occurs, as identified by means of Ducros sensor [21, 11]. The time integration is performed with a maximum Courant-Friedrichs-Lewy number CFL of 11, and the non-linear system is solved through 7 sub-iterations resulting in a reduction of the residuals of more than three orders of magnitude in the laminar and transitional regions and about two orders of magnitude in the turbulent ones. The LES modeling is built from an implicit grid filtering coupled with an explicit subgrid modeling through the selective mixed-scale model [14, 1]. The reference meshes are $\Delta x^+ \lesssim 30$, $\Delta z^+ \lesssim 15$ and $y_1^+ \lesssim 1.25$ and the width of the computational domain is 7 times larger than the separation bubble height. Additional meshes refined by 40%, 20% and 25% in the x , y and z directions have been built in order to perform a grid convergence study. For the sole IUSTI case, a mesh enlarged in the spanwise direction by 100% has also been tested.

The wall is treated as adiabatic, and periodicity is used

Table 1: Flow parameters.

Case	Mach	Re_{imp}	θ	L/δ_{imp}^*
IUSTI	1.68	6.5×10^5	4.96°	4.02
TU Delft	1.70	1.85×10^6	3.00°	1.92

in the spanwise direction. Non-reflecting boundary conditions based on characteristics formulation are set at the inflow, outflow and upper boundaries. The inflow conditions are obtained by superimposing flow perturbations of very low amplitude and large bandwidth to the compressible Blasius profile by means of a compressible variant of the Synthetic Eddy Method (SEM) [16]. However, the amplitude of these perturbations were not known from the experiments. The strategy followed was to adjust them iteratively such that the final computations result in the same separation length as the experiments. The simulations were run long enough to encompass 70 and 25 cycles of the typical low-frequency unsteadiness for the IUSTI and TU Delft cases respectively allowing the computation of spectral quantities.

2.2 Validation

Computations for both cases have been compared to experimental measurements obtained through LDV (IUSTI) and micro-PIV (TU Delft) techniques. The validation accounts for refined meshes in all of the directions as described in Sec. 2.1, and for the sole IUSTI case a mesh enlarged in the spanwise direction has also been validated. Fig. 1 plots the mean streamwise velocity profiles at different streamwise locations. The streamwise coordinate is defined as the distance between the impingement location of the incident shock x_{imp} and the current location x and it is normalised by the incoming boundary layer thickness δ_{99} . The wall-normal coordinate is normalised by using the same reference length. All the profiles collapse demonstrating that the procedure described in Sec. 2.1 regarding the adjustment of the inflow perturbations amplitude is successful.

Experimental and numerical data show excellent agreement up to the apex of the recirculation bubble. Nonetheless, experiments tend to yield transition downstream of the apex. The transition phenomena occurs more abruptly over a shorter distance, resulting in quicker relaxations towards a canonical turbulent boundary layer downstream of the interaction region. It is unclear if this discrepancy is due to either the different physical nature of the perturbations in the incoming boundary layer or an alteration of the transition mechanism within the bubble due to the LES modelling. The fact that no difference is observed between the base computations and the ones relying on the refined meshes, even downstream of the apex, is an indication that the former hypothesis is more

likely.

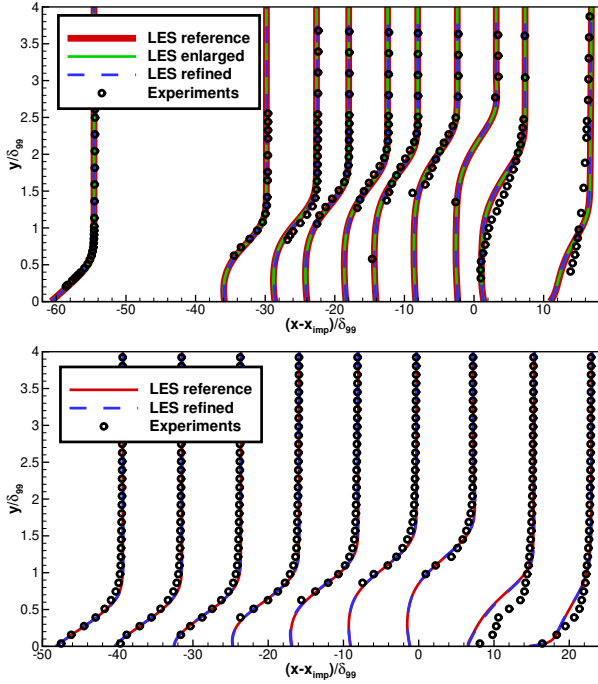


Figure 1: Comparison of the mean streamwise velocity profiles between experiments and computations at different streamwise locations: IUSTI case (upper panel) and TU Delft case (lower panel).

3. RESULTS

3.1 Linear spectral analysis

The time spectral analysis is considered to identify the key features of the shock motion and the characteristic temporal scales are extracted through spectral decomposition of wall pressure fluctuations. From this section onwards, the streamwise location is normalised by using the interaction length L defined as the distance between the impingement location x_{imp} of the incident shock and the beginning of the interaction region x_{int} . The latter position has been defined by extrapolating the center of the compression region down to the wall. The normalised streamwise coordinate then reads:

$$x^* = \frac{x - x_{int}}{L} \quad (1)$$

In this way the interaction region ranges from 0 to 1. Instead the frequency is normalised by the interaction length scale L , as defined above, and the free-stream velocity U_∞ , corresponding to the Strouhal number:

$$St_L = \frac{fL}{U_\infty} \quad (2)$$

Fig. 2 shows the streamwise distributions of the pre-multiplied, normalised wall pressure spectra for the IUSTI (upper panel) and TU Delft (lower panel) cases. The separation $x^* = 0$ and the reattachment $x^* = 1$ points are marked with white horizontal dashed lines while the vertical ones correspond to meaningful Strouhal numbers, as will be explained in this section. Both spectra show that the beginning of the interaction, near $x^* = 0$, is dominated by energy content spread at low frequencies, with typical Strouhal number of $St_L \simeq 0.055$ (see white vertical dashed line in the figures). This value is close to the one found in the DNS by [23] and LES by [17], but it is significantly lower than the $St_L \simeq 0.1$ value seen in the experiments by [8]. Conversely, the work of [4] yields an intermediate values of $St_L \simeq 0.08$. Such discrepancies in the low-frequency Strouhal numbers may be related to different physical forcing strategies of the incoming boundary layer/initial mixing layer adopted by the aforementioned works. In fact, the present LES, the LES of [17] and the DNS of [23] rely on rather similar forcing mechanism of the incoming boundary layer whereas the RANS in [4] use a different approach. However, some differences emerge when comparing the separation region of the two cases. In the IUSTI case, the energetically dominant low-frequency content extends to the $St_L \simeq 0.03$ (see the upper panel in Fig. 2). This value has been observed in [12] and more recently in the study of [24], but for a fully turbulent interaction. It is localised around the separation point $x^* = 0$, unlike in the TU Delft spectrum. In fact, the lower panel of Fig. 2 exhibits a concentrated narrow energetic low-frequency content extending downstream within the separation bubble, and no spreading down to $St_L \simeq 0.03$ is observed. The reason will be clear in Sec. 3.2.

Back to the Fig. 2, the typical frequency increases up to $St_L \simeq 1$ moving in the streamwise direction towards the reattachment point $x^* = 1$. Once past this point, a bump of high energy content emerges in both spectra. In the IUSTI case, it is localised in the region of the flow downstream the reattachment point at $x^* \simeq 1.1$ and the associated Strouhal number is $St_L \simeq 2$ (see the white circle in the upper panel of Fig. 2). On the contrary, the TU Delft bump shifts towards the reattachment point $x^* = 1$ and the corresponding Strouhal number is $St_L \simeq 1$. Such a difference in the positions and Strouhal numbers is due to the relative dimension of the separated region based on the displacement thickness that differs in the two cases (see Tab. 1). The presence of the bump has already been observed in the work of [17] which investigated transitional SBLIs, but no evidence have been reported for the turbulent counterpart. Its rise is explained below. In the first part of the recirculating region, eddies develop in the mixing layer zone and grow as it moves downstream. After some distance, these eddies are shed into the downstream flow, possibly leaving their trace at the wall. How-

ever, previous studies demonstrated that eddies remain at a certain distance from the wall, making the previous statement weak as the only explanation. Moreover, the mechanism just described is also common in turbulent interactions, where the emergence of such a bump is not documented (see for example [24]). Therefore, other features have to take into account. The position $x^* \simeq 1.1$ is associated with the location where transition to turbulence occurs (results are not shown here). So, more than a footprint of the mixing layer structures, this bump could represent the trace of the transition process. In addition, the bump could be related to the breakdown of oblique instability modes originating from the initial mixing layer and propagating downstream to the reattachment point. They play a fundamental role in explaining the origin of low-frequency unsteadiness, as will be demonstrated in Sec. 3.2.

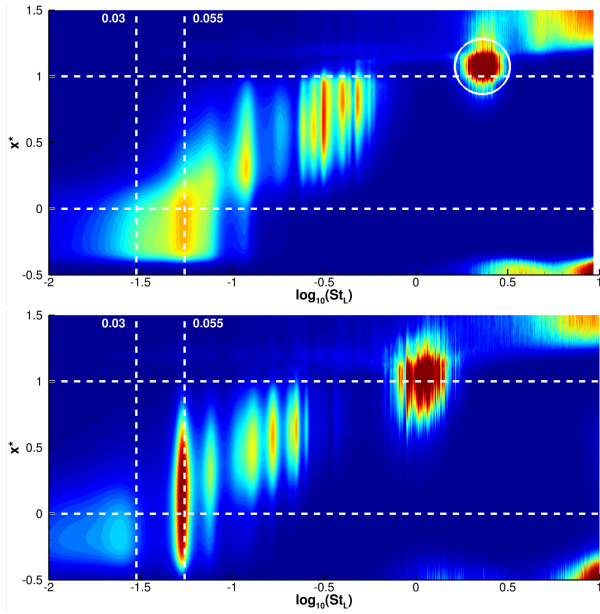


Figure 2: Streamwise evolution of the premultiplied, normalised wall pressure spectrum: IUSTI case (upper panel) and TU Delft case (lower panel). White horizontal dashed lines mark separation $x^* = 0$ and reattachment $x^* = 1$ points while the vertical ones correspond to Strouhal numbers $St_L \simeq 0.03$ and $St_L \simeq 0.055$. The white circle in the IUSTI case denotes the high-energetic content associated with the transition and breakdown of oblique instability modes.

From the previous analysis, the position where the bump emerges seems to be critical to define the source of the low-frequency unsteadiness. A more deep investigation has been conducted by resorting to the phase information from the two-points spectrum. The cross-spectrum is a complex valued quantity defined as:

$$S_{g_1, g_2}(f) = G_1(f) G_2^*(f) \quad (3)$$

where $G_1(f)$ and $G_2(f)$ are the Fourier transforms of the time series $g_1(t)$ and $g_2(t)$ respectively, while $*$ denotes the complex conjugated.

In this work, the wall pressure cross-spectrum for the IUSTI case has been computed. The separation location $x^* = 0$ is the reference point and all the possible linear links between pressure signals at the wall along the streamwise direction are obtained. From the cross-spectrum, phase information is extracted for three regions, *i.e.* point of separation, inside the separation bubble and near the reattachment point, based on their characteristic Strouhal number, *i.e.* $St_L \simeq 0.055$, $St_L \simeq 0.33$ and $St_L \simeq 2$ respectively. Fig. 3 plots the streamwise evolution of the normalised phase at the fixed aforementioned Strouhal numbers. Note that the phase data are unwrapped so that jumps of 2π are removed. The inverse of the curves slope gives information regarding the phase velocity between the reference and the selected wall pressure signals as well as the direction of travelling. The phase velocity reads:

$$V_\Phi = \frac{2\pi f \Delta x}{\Delta \Phi} \quad (4)$$

where $\Delta x = x - x_{sep}$ and $\Delta \Phi$ is the phase shift between the two wall pressure signals. It is important to point out that the phase velocity is associated with a fixed frequency, but is contaminated by all the streamwise wavenumbers k_{x_i} . Not having selected a particular wavenumber, one can assume that rather than the phase velocity, what is observed is the average velocity at which the group of signals characterised by a given frequency is traveling, *i.e.* the group velocity V_g . By assuming $V_\Phi \sim V_g \sim U_c$ where U_c is the convection velocity, Fig. 3 provides the follow information. For $St_L \simeq 2$, the phase increases linearly throughout the streamwise direction. The convection velocity is $U_c \simeq 0.5U_\infty$ meaning that the pressure waves are travelling from upstream towards downstream regions with respect to the separation point. However, for lower Strouhal numbers an abrupt change in phase is observed at $x^* \simeq 1.1$. In particular, up to $x^* \simeq 1.1$, the phase decreases nearly linearly while it increases linearly everywhere else. Before the jump, upstream propagation velocities are found which values correspond to $U_c \simeq -0.24U_\infty$ and $U_c \simeq -0.41U_\infty$ for the low and the medium frequencies respectively. After the jump, downstream propagation speeds are observed. From this scenario it is possible to infer that the source of the slow-upstream propagating pressure waves is located at $x^* \simeq 1.1$ where the bump previously observed emerges (see Fig. 2). Reference [25] reported similar conclusions for a turbulent interaction, although the location of the low-frequency was found laying about one third of the way down the bubble.

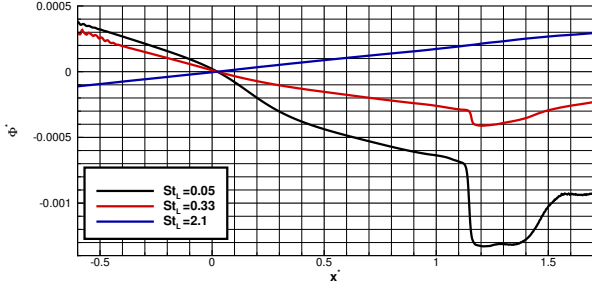


Figure 3: IUSTI case: streamwise evolution of the normalised phase for three selected Strouhal numbers, *i.e.* $St_L \simeq 0.055$, $St_L \simeq 0.33$, and $St_L \simeq 2$

3.2 Non-linear spectral analysis

Two-points spectral analysis revealed that the origin of the low-frequency breathing of the separation bubble corresponds to the location where the bump emerges. Moreover, [band-pass filtered pseudo-schlieren movies](#) shows the occurrence of a fluidic feedback starting from the reattachment point for $St_L \lesssim 1$. It progressively restricts to a narrower low-frequency band while moving upstream. Highly energetic fluctuations are also visible in the vicinity of the reattachment point for much higher frequencies. Therefore, multiple mechanisms are at play in this region, including transition and quadratic interactions that might trigger beating between different frequencies.

However, the second-order statistics are only sufficient for describing linear processes. To detect and quantify non-linearities in time series, high-order statistics are required. In that context, bispectrum and bicoherence information are used to propose a scheme explaining how energy at low-frequency appears near the reattachment point before being convected upstream, then inducing the breathing of the bubble.

The region of the flow around the reattachment point is dominated by large-scale motions whose frequencies, as seen on the bump at $St_L \simeq 2$, $x^* \simeq 1.1$, are much higher than the low-frequency range associated with the upstream feedback. Because of the frequencies difference, both phenomena cannot be linearly linked but they can be related through quadratic interactions. Such interactions can be highlighted in the spectral space from the bispectrum, which is a measure of the quadratic non-linearities at the bifrequency (f_1, f_2) [28, 6]. One way to normalise the complex-valued bispectrum is the bicoherence between time series $g_1(t)$, $g_2(t)$ and $g_3(t)$, which reads:

$$Bic_{g_1, g_2, g_3}(f_1, f_2) = \frac{\|G_1(f_1) G_2(f_2) G_3^*(f_1 + f_2)\|^2}{\|G_1(f_1) G_2(f_2)\|^2 \|G_3(f_1 + f_2)\|^2} \quad (5)$$

where $G(f)$ denotes the Fourier transform of the time series $g(t)$. A value of Bic_{g_1, g_2, g_3} that differs significantly

from zero is associated with a (partial) phase relationship between $g_1 \times g_2$ and g_3 being stable over time, and it is indicative of possible non-linear energy exchange between the frequencies under consideration.

In the present work, the analysed variable is the streamwise momentum ρu since it may experience quadratic interactions through the convective term of the Navier-Stokes momentum equation. Fig. 4 shows the locations where ρu has been sampled, corresponding to the end of the ascending mixing layer ($S1$), the center of the descending mixing layer ($S2$) and three locations distributed on a horizontal line fairly close to the wall, either upstream of, at, or downstream of the reattachment point ($S3$, $S4$ and $S5$ respectively). Fig. 5 plots the bicoherence map between $S1 \times S1$ and $S2$ for the IUSTI case and the presence of strong bicoherence identifies those frequency modes that most strongly contribute towards the quadratic phase coupling (QPC). The linearly unstable modes develop in the ascending mixing layer and enter the non-linear regime near the apex of the bubble. Indeed, the positive quadrant of the bicoherence map is typical of a transitioning mixing layer. It displays an emerging direct turbulent cascade involving triadic interaction between frequency ranges being integer multiples of the original instability wave range at location $S1$, centered around $St_L \simeq 2$. On the contrary, quadrant defined by $St_{L1} < 0$ and $St_{L2} > 0$ displays a quadratic link towards lower-frequencies with $|St_{L1}| \simeq |St_{L2}|$. Spots of higher values of bicoherence for very low values of Strouhal numbers are observed.

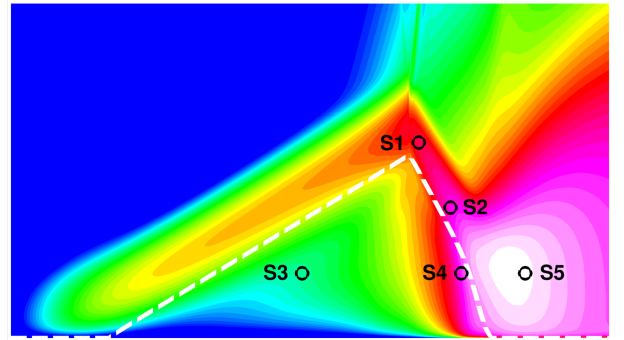


Figure 4: S_i indicates the location of the sensors used in the bispectral analysis superimposed to exponentially-spaced filled isolevels of turbulent kinetic energy and to the mean dividing streamline indicated with white dashed line.

For triadic interactions between band-limited signals such as the ones centered around $St_L \simeq 2$, bicoherence is rather easy to analyse. However, such an analysis may become trickier for more broadband signal since a single frequency can be involved in multiple triadic interactions. One way to overcome this difficulty is to use the summed bicoherence, defined as:

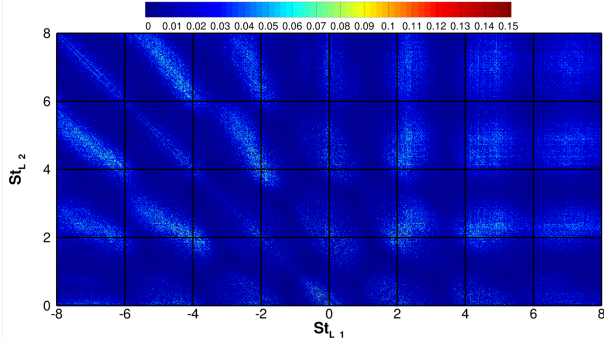


Figure 5: IUSTI case: bicoherence map between $S1 \times S1 \leftrightarrow S2$.

$$\Sigma bic_{g_1, g_2, g_3}(f) = \frac{\sum_{|f_1+f_2|=f} \|G_1(f_1) G_2(f_2) G_3^*(f_1+f_2)\|^2}{\sum_{|f_1+f_2|=f} \|G_1(f_1) G_2(f_2)\|^2 \|G_3(f_1+f_2)\|^2} \quad (6)$$

Summed bicoherence plots between the “source” signal $S1 \times S1$ and streamwise momentum at different locations are displayed in Fig. 6. The cascade process for sensors $S2$ and $S4$ that are located at the center of, and near to the wall of the descending mixing layer is shown in the upper panel of Fig. 6. The energy transfer towards higher harmonics of the original instability wave at $St_L \simeq 2$ seen in the positive quadrant of Fig. 5, is mostly achieved when approaching the vicinity of the reattachment point (see sensor $S2$). Once the reattachment location is reached, the turbulence is close to be fully developed and only short-range triadic interactions are observed (see sensor $S4$). However, an energy transfer towards the low-frequency range takes place within the separation bubble, as sensor $S3$ shows in the lower panel of Fig. 6. For this range of low-frequency, the linear analysis revealed an upstream motion as pointed out with Fig. 3. No such process is identified downstream of the reattachment point as sensor $S5$ shows. It is worth noting that the relative energy content at low-frequency is increasing when moving upstream within the bubble.

Based on these results, it can be postulated that the upstream low-frequency feedback is triggered by quadratic interactions between high-frequency oblique modes found in the mixing layer developing over the separated region. This scenario is in agreement with several numerical studies of TrSWBLI. Such a mechanism would also be consistent with the lack of low-frequency unsteadiness observed when the interaction is fully laminar.

Information obtained for the IUSTI case are confirmed when applying the same non-linear postprocessing to the unsteady data gathered from the simulation of the TU Delft case. Bispectral quantities involving data sampled

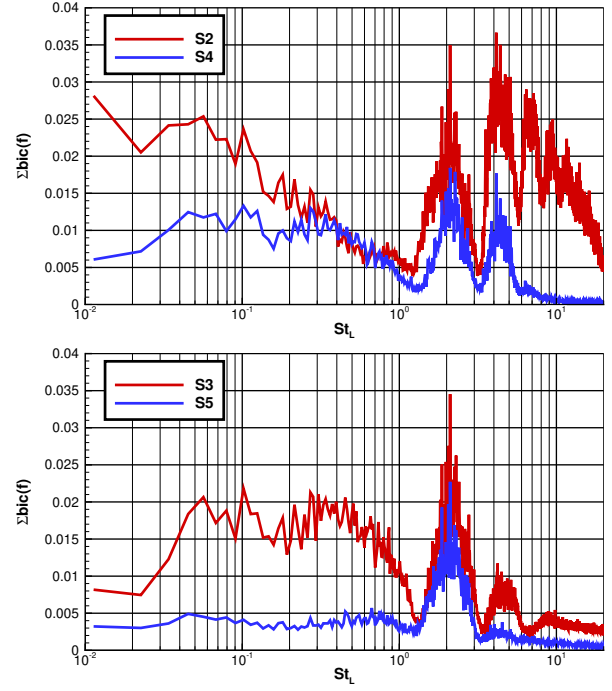


Figure 6: IUSTI case: summed bicoherence with $S1 \times S1$ for sensors located within the descending shear layer (upper panel) and near the wall, both upstream and downstream of the reattachment point (lower panel).

from sensors $S1$ to $S5$, similarly located with respect to the geometry of the separated region as for the IUSTI case, have been computed. The bicoherence map related to the quadratic coupling $S1 \times S1 \leftrightarrow S2$ is plotted in the upper panel of Fig. 7. Note that the value of contour levels have been increased to reflect the increase of the statistical significance threshold for the bicoherence due to the lower number of samples used for the TU Delft case. The region of positive St_{L1} shows a less evident direct cascade with respect to the IUSTI case. In fact, the bicoherence map displays only few spots from frequency $St_1 \simeq 1$ towards higher frequencies (recall that $St_1 \simeq 1$ is associated with the mixing layer modes for the TU Delft case). It may be explained by the fact that sensor $S2$ in the TU Delft case is located closer to the wall than its counterpart in the IUSTI setup for practical sampling reasons. Therefore, the initial phase of the direct cascade from $St_L \simeq 1$ towards $St_L \simeq 2 \times 1$ has already been completed at this location. The largest value of the Reynolds number in the TU Delft setup, resulting in a transition occurring over a shorter distance, may also play a role. The $(St_{L1} < 0, St_{L2} > 0)$ quadrant is quite similar to the one observed for the IUSTI case. Interactions between mixing layer oblique modes and the product of higher frequencies are strong. In addition, interactions from the low frequency range with product of higher frequencies, among which are the mixing layer modes at $St_L \simeq 1$, are

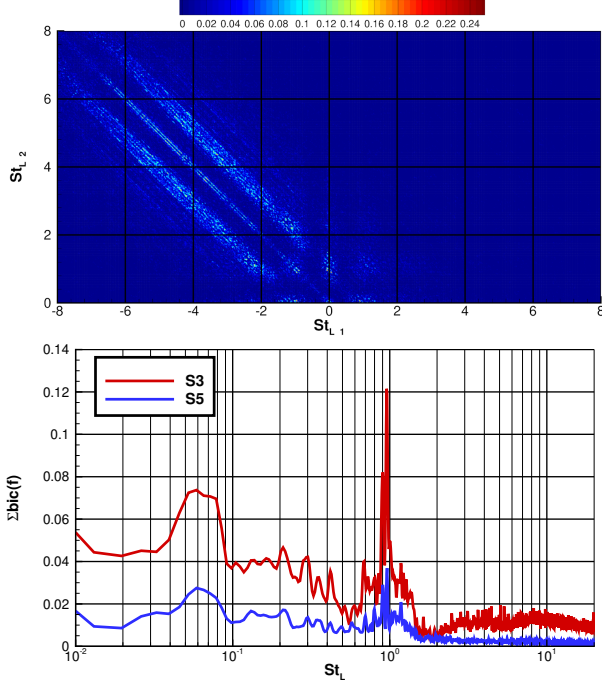


Figure 7: Bispectral analyses for the TU Delft case: bicoherence map $S_1 \times S_1 \leftrightarrow S_2$ (upper panel) and summed bicoherence with $S_1 \times S_1$ for sensors located near the wall, both upstream and downstream of the reattachment point (lower panel).

also significant. It is worth noting that the low-frequency range is narrower than for the IUSTI case. It is consistent with the narrow energetically prevalent range at $St_L \simeq 0.05$ visible in the lower panel of Fig. 2. Lastly, the summed bicoherence is shown in the lower panel of Fig. 7. Sensors are located in the vicinity of the wall, either within the separated region (S3) or downstream of it (S5). The plot highlights a significant quadratic link at low-frequency between the “source” sensor S1 and the one located in the separated region, *i.e.* sensor S3. Once again, this is mostly similar to what observed for the IUSTI case in the lower panel of Fig. 6, with the difference of a narrower low-frequency band. The reduced bandwidth of the low-frequency region for the TU Delft case has more likely to be related to the lower relative size of the separated bubble with respect to the incoming boundary layer than to the higher value of the Reynolds number.

Bicoherence spectra convey information on the quadratic link between various regions of the flow, but do not provide any data regarding motion within these regions. However, information on the convective or stationary nature of the quadratic link can be recovered from the biphas spectrum using the same methodology developed in Sec. 3.1 for the cross-spectrum. The biphas spectrum correspond to the argument of the complex-valued

bispectrum $G_1(f_1) G_2(f_2) G_3^*(f_1 + f_2)$. For a given frequency pair (f_1, f_2) , it is a measure of the phase difference between part of the g_3 series considered at frequency $f_1 + f_2$ that is quadratically linked with part of the product between g_1 and g_2 , considered at frequencies f_1 and f_2 respectively. In other words, it is the phase difference of the portions of $G_3(f_1 + f_2)$ and $G_1(f_1) \times G_2(f_2)$ that are phase-locked over time and in the spanwise homogeneous direction, as denoted by a significant value of the bicoherence $Bic_{g_1, g_2, g_3}(f_1, f_2)$.

The streamwise evolution of the biphas between the $S1 \times S1$ sensors and sensors distributed over a horizontal line crossing sensors S3 to S5 is plotted in Fig. 8. High-frequency frequency pairs whose sums correspond either to the various typical low-frequency Strouhal fluctuations identified in the separated region ($St_{L3} < 1$) or to the oblique modes and their harmonics ($St_{L3} \simeq n \times 2.1, n \in \mathbb{N}$) have been selected. Among the various frequency pairs of a given sum that have been computed, the three ones resulting in the largest bicoherence levels have been retained. In that sense, the streamwise phase evolution being plotted is representative of the strongest quadratic contributions to the low-frequency range.

Comparison of Fig. 3 and Fig. 8 confirms that in the initial region of the interaction up to $x^* \simeq 0.5$ the phase evolution in both cases is very similar for the frequency range under consideration. As a consequence, the group velocity associated with the motion of the fluctuations quadratically linked with the oblique mode is roughly the same as the one found from the linear two-point analysis. This, coupled with the rather large values of bicoherence found in that region, confirms that the upstream-convected momentum fluctuations are for a large part induced by non-linear coupling with the mixing layer oblique modes. Since such an upstream motion has been associated with the low-frequency breathing of the separated region, it is therefore strongly suggested that the breathing is induced by non-linear beating in the vicinity of the reattachment point of the high-frequency oblique modes having developed within the mixing layer. Such a scheme could explain the lack of low-frequency breathing in the case of fully laminar interaction, for which quadratic interactions of modes are poorly energetic and do not result in transition.

4. CONCLUSIONS

LES computations of two transitional SBLIs with separation have been carried out and compared with experimental databases from the TFAST project. All computations have been validated resulting in an excellent agreement between experimental and numerical data. The high-order statistics tools in the spectral space have been used to explore the linear and quadratic interactions responsible for the origin of the low-frequency unsteadiness.

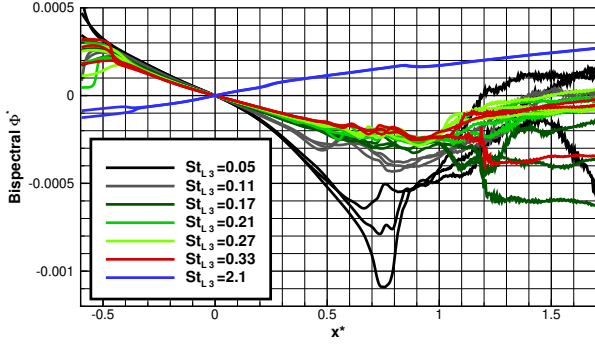


Figure 8: IUSTI case: streamwise evolution of the normalised biphase along the horizontal line crossing sensors S3 to S5. For each St_{L_3} spanning from low to high values, the three combinations resulting in the highest values of the bicoherence are plotted.

The two-points linear spectral analysis confirmed the occurrence of a slow-upstream convection motion originating from the vicinity of the reattachment point $x^* \simeq 1.1$ where a bump of high-energy content emerges. The low-frequency range in the separated region was found to be also significantly quadratically linked with the oblique mixing layer modes of much higher frequencies, as pointed out from bicoherence spectra. The biphase diagnostic then confirmed that such a long-range quadratic link is indeed related to the downstream-to-upstream fluidic feedback.

5. ACKNOWLEDGMENTS

This work was supported by TEAMAero Horizon 2020 research and innovation program under grant agreement 860909.

This work was granted access to the HPC resources of CINES and IDRIS under the allocations A0022A01877, A0062A01877 and A0102A01877 made by GENCI.

REFERENCES

- [1] L. Agostini, L. Larchevêque, and P. Dupont. Mechanism of shock unsteadiness in separated shock/boundary-layer interactions. *Physics of Fluids*, 27:126103, 2015.
- [2] L. Agostini, L. Larchevêque, P. Dupont, J. F. Debiève, and J. P. Dussauge. Zones of influence and shock motion in a shock/boundary-layer interaction. *AIAA Journal*, 50:1377–1387, 2012.
- [3] H. Babinsky and J. K. Harvey. *Shock wave-boundary-layer interactions*. Cambridge, UK, 2011.
- [4] V. Bonne, N. Brion, E. Garnier, R. Bur, P. Molton, D. Sipp, and L. Jacquin. Analysis of the two-dimensional dynamics of a mach 1.6 shock wave/transitional boundary layer interaction using a rans based resolvent approach. *Journal of Fluid Mechanics*, 862:1166–1202, 2019.
- [5] N. T. Clemens and V. Narayanaswamy. Low-frequency unsteadiness of shock wave/turbulent boundary layer interactions. *Annual Review of Fluid Mechanics*, 46:469–492, 2014.
- [6] G. Cui and I. Jacobi. Biphasic as a diagnostic for scale interactions in wall-bounded turbulence. *Physical Review Fluids*, 6:014604, 2021.
- [7] M. Diop, S. Piponniau, and P. Dupont. On the length and time scales of a laminar shock wave boundary layer interaction. In *54th AIAA Aerospace Sciences Meeting*, 2016.
- [8] M. Diop, S. Piponniau, and P. Dupont. High resolution lda measurements in transitional oblique shock wave boundary layer interaction. *Experiments in Fluids*, 60:57, 2019.
- [9] D. S. Dolling. Fifty years of shock-wave/boundary-layer interaction research: What next? *AIAA Journal*, 8:1517–1531, 2001.
- [10] D. S. Dolling and M. T. Murphy. Unsteadiness of the separation shock wave structure in a supersonic compression ramp flowfield. *AIAA Journal*, 21:1628–1634, 1983.
- [11] F. Ducros, V. Ferrand, F. C. Nicoud, Weber, D. Daracq, C. Gacherieu, and T. Poinot. Large-eddy simulation of the shock/turbulence interaction. *Journal of Computational Physics*, 152:517–549, 1999.
- [12] P. Dupont, C. Haddad, and J. F. Debiève. Space and time organization in a shock-induced separated boundary layer. *Journal of Fluid Mechanics*, 559:255–277, 2006.
- [13] B. Ganapathisubramani, N. T. Clemens, and Dolling D. S. Low-frequency dynamics of shock-induced separation in a compression ramp interaction. *Journal of Fluid Mechanics*, 636:397–425, 2009.
- [14] E. Garnier, P. Sagaut, and M. Deville. Large eddy simulation of shock/boundary-layer interaction. *AIAA Journal*, 40:1935–1944, 2002.
- [15] R. H. M. Giepmans, F. F. J. Schrijer, and B. W. van Oudheusden. A parametric study of laminar and transitional oblique shock wave reflections. *Journal of Fluid Mechanics*, 844:187–215, 2018.

- [16] N. Jarrin, S. Benhamadouche, D. Laurence, and R. Prosser. A synthetic-eddy-method for generating inflow conditions for large-eddy simulations. *International Journal of Heat and Fluid Flow*, 27:585–593, 2006.
- [17] L. Larchevêque. Low- and medium-frequency unsteadinesses in a transitional shock–boundary reflection with separation. *54th AIAA Aerospace Sciences Meeting*, 2016.
- [18] S. Piponniau, J. P. Dussage, J. F. Debiève, and Dupont P. A simple model for low-frequency unsteadiness in shock-induced separation. *Journal of Fluid Mechanics*, 629:87–108, 2009.
- [19] S. Pirozzoli and F. Grasso. Direct numerical simulation of impinging shock wave/turbulent boundary layer interaction at $m=2.25$. *Physics of Fluids*, 065113, 2006.
- [20] S. Priebe and M. Pino Martín. Low-frequency unsteadiness in shock wave–turbulent boundary layer interaction. *Journal of Fluid Mechanics*, 699:1–49, 2012.
- [21] P. L. Roe. Approximate riemann solvers, parameter vectors, and difference schemes. *Journal of Computational Physics*, 43:357–372, 1981.
- [22] A. Sansica, N. D. Sandham, and Z. Hu. Forced response of a laminar shock-induced separation bubble. *Physics of Fluids*, 26:093601, 2014.
- [23] A. Sansica, N. D. Sandham, and Z. Hu. Instability and low-frequency unsteadiness in a shock-induced laminar separation bubble. *Journal of Fluid Mechanics*, 798:5–26, 2016.
- [24] K. Sasaki, D. C. Barros, A. V. G. Cavalieri, and L. Larchevêque. Causality in the shock wave/turbulent boundary layer interaction. *Physical Review Fluids*, 6:064609, 2021.
- [25] E. Toubert. *Unsteadiness in Shock-Wave/Boundary Layer Interactions*. PhD thesis, University of Southampton, 2010.
- [26] E. Toubert and Sandham N. D. Large-eddy simulation of low-frequency unsteadiness in a turbulent shock-induced separation bubble. *Theoretical and Computational Fluid Dynamics*, 23:79–107, 2009.
- [27] E. Toubert and Sandham N. D. Low-order stochastic modelling of low-frequency motions in reflected shock-wave/boundary-layer interactions. *Journal of Fluid Mechanics*, 671:417–465, 2011.
- [28] G. R. Tynan, R. A. Moyer, M. J. Burin, and C. Holland. On the nonlinear turbulent dynamics of shear-flow decorrelation and zonal flow generation. *Physics of Plasmas*, 8:2691–2699, 2001.
- [29] M. Wu and M. Pino Martín. Analysis of shock motion in shockwave and turbulent boundary layer interaction using direct numerical simulation data. *Journal of Fluid Mechanics*, 594:71–83, 2008.